The Astrophysical Journal, 779:178 (13pp), 2013 December 20 doi:10.1088/0004-637X/779/2/178

THE ATOMIC AND MOLECULAR CONTENT OF DISKS AROUND VERY LOW-MASS STARS AND BROWN DWARFS

I. Pascucci[1], G. Herczeg[2], J. S. Carr[3], and S. Bruderer[4]
[1] Lunar and Planetary Laboratory, The University of Arizona, Tucson, AZ 85721, USA; pascucci@lpl.arizona.edu
[2] Kavli Institute for Astronomy and Astrophysics, Peking University, Beijing 100871, China
[3] Naval Research Laboratory, Code 7211, Washington, DC 20375, USA
[4] Max Planck Institute for Extraterrestrial Physics, Giessenbachstrasse 1, D-85748 Garching, Germany
Received 2013 June 6; accepted 2013 October 29; published 2013 December 4

ABSTRACT

There is growing observational evidence that disk evolution is stellar-mass-dependent. Here, we show that these dependencies extend to the atomic and molecular content of disk atmospheres. We analyze a unique dataset of high-resolution *Spitzer*/IRS spectra from eight very low mass star and brown dwarf disks. We report the first detections of Ne^+, H_2, CO_2, and tentative detections of H_2O toward these faint and low-mass disks. Two of our [Ne II] 12.81 μm emission lines likely trace the hot ($\geqslant$5000 K) disk surface irradiated by X-ray photons from the central stellar/sub-stellar object. The H_2 $S(2)$ and $S(1)$ fluxes are consistent with arising below the fully or partially ionized surface traced by the [Ne II] emission in gas at $\sim$600 K. We confirm the higher C_2H_2/HCN flux and column density ratio in brown dwarf disks previously noted from low-resolution IRS spectra. Our high-resolution spectra also show that the HCN/H_2O fluxes of brown dwarf disks are on average higher than those of T Tauri disks. Our LTE modeling hints that this difference extends to column density ratios if H_2O lines trace warm $\geqslant$600 K disk gas. These trends suggest that the inner regions of brown dwarf disks have a lower O/C ratio than those of T Tauri disks, which may result from a more efficient formation of non-migrating icy planetesimals. An O/C = 1, as inferred from our analysis, would have profound implications on the bulk composition of rocky planets that can form around very low mass stars and brown dwarfs.

Key words: accretion, accretion disks – brown dwarfs – protoplanetary disks – stars: low-mass – stars: pre-main sequence

Online-only material: color figures

1. INTRODUCTION

The mass and lifetime of gas in protoplanetary disks affect the formation and evolution of both giant and terrestrial planets. The connection to giant planets is perhaps the most obvious: giant planets must accrete most of their atmospheres from nebular gas, hence the gas disk lifetime constrains their formation time (e.g., Lissauer & Stevenson 2007). Once formed, giant planets can also migrate, as evinced by the detection of hot Jupiters around nearby stars (e.g., Howard et al. 2012). This migration can only occur in the presence of disk gas, and the migration timescale strongly depends on the gas disk mass (Papaloizou & Terquem 2006). In addition, giant planet atmospheres reflect the disk gas-phase abundance at their formation sites, if contamination from planetesimal accretion is minimal. Öberg et al. (2011) discuss how the C/O ratio in hot Jupiters depends on the disk chemistry and the different snow lines of major carbon- and oxygen-bearing species; this ratio can be used to infer the radial distances at which hot Jupiters formed. Terrestrial planets are thought to form later than giant planets, likely in a gas-poor environment (e.g., Nagasawa et al. 2007). However, residual gas might help circularize their orbits (Kominami & Ida 2002) and determine their water content by transporting inward icy solids that can accrete onto forming terrestrial planets (e.g., Ciesla & Lauretta 2005). Similarly to water, carbon is not accreted by in situ formation models of Earth and may be delivered by accretion of icy bodies formed beyond the snowline (Bond et al. 2010; Lee et al. 2010).

In spite of its relevance to planet formation and the architecture of planetary systems, the amount, composition, and evolution of gaseous disks is poorly understood. Mid-infrared observations with the *Spitzer Space Telescope* (hereafter, *Spitzer*) are enabling for the first time the study of disk gas atmospheres at radial distances where terrestrial and giant planets are expected to form.

The first detailed analysis of high-resolution ($R \sim 700$) *Spitzer* spectra from three accreting sun-like stars (hereafter, T Tauri stars) revealed many rotational transitions from H_2O vapor and OH as well as rovibrational emission bands from simple organic molecules such as C_2H_2 and HCN (Carr & Najita 2008; Salyk et al. 2008). Similar analyses extended to larger samples suggest that H_2O is abundant in the inner few AU of T Tauri disks and traces a limited range of temperatures and column densities (Carr & Najita 2011; Salyk et al. 2011). This limited range of excitation conditions is revealed by the similar relative strength of H_2O lines measured from star to star. In contrast, the relative strengths of different organic molecules, and their strengths with respect to water, present a much broader range. Carr & Najita (2011) propose that the range in HCN/H_2O strength, in particular, results from different C/O ratios in the inner disk as a result of the migration history of icy planetesimals (see also Najita et al. 2013). This explanation hints that the composition of the gas disk atmosphere reflects radial transport in the disk midplane and perhaps planet formation timescales. On the other hand, the relative changes of H_2O and OH in the *Spitzer* spectra of the strongly variable T Tauri star EX Lupi points to stellar UV radiation as a key parameter for the disk surface chemistry (Banzatti et al. 2012). Similarly, stellar UV irradiation has been invoked to explain the lack of H_2O lines in *Spitzer* spectra of Herbig Ae/Be stars, which contrasts with two-thirds of T Tauri disks having detectable water emission (Pontoppidan et al. 2010; see also Fedele et al.

Table 1
Summary of Source Properties

ID	2MASS J	Other Name	SpTy	d (pc)	Mass ($M_\odot$)	Log(L_{bol}) ($L_\odot$)	Log(M_{acc}) ($M_\odot$ yr^{-1})	Log(L_X) (erg s^{-1})	Log(L_{FUV}) ($L_\odot$)	Ref.
1	04381486+2611399		M7.25	140	0.07	−2.3	−10.8	...	...	1,2,3,4
2	04390163+2336029	[SCH2006b] J0439016+2336030	M6	140	0.08	−1.0	...	...	−5.25	1,2,4,5,6
3	04390396+2544264		M7.25	140	0.05	−1.7	−11.2	...	...	1,2,3
4	04442713+2512164		M7.25	140	0.05	−1.3	...	27.6–28.6	−4.93	1,2,4,5,6,7
5	05180285+2327127	[SCH2006b] J0518028+2327126	M5.5	140	0.1	0.02	...	...	−3.67	2,5,6
6	15582981−2310077	UScoCTIO 33	M4.5	145	0.16	−1.5	−9.2	...	...	8,9
7	16053215−1933159		M4.5	145	0.16	−1.4	−9.1	...	...	8,9
8	16222160−2217307	[SCH2006] J16222156−22173094	M5	145	0.11	−2.0	...	...	...	8,10

References. (1) Luhman et al. 2010; (2) Kenyon et al. 2008; (3) Muzerolle et al. 2005; (4) Rebull et al. 2010; (5) Herczeg & Hillenbrand 2008; (6) Yang et al. 2012; (7) Güdel et al. 2007; (8) de Zeeuw et al. 1999; (9) G. Herczeg et al. (in preparation); (10) Slesnick et al. 2006.

Table 2
Log of the Observations

ID	2MASS J	AOR Key	PID	SH (time[a] × ncycles)	SL (time[a] × ncycles)	LL (time[a] × ncycles)
1	04381486+2611399	26924288,12705792	50799,2	120 × 10	60 × 12	...
2	04390163+2336029	26925824	50799	120 × 10	14 × 2	14 × 2
3	04390396+2544264	26924800,18353664	50799,30540	120 × 8	60 × 1	30 × 8
4	04442713+2512164	26925312,12708608	50799,2	120 × 8	14 × 2	30 × 2
5	05180285+2327127	26926336	50799	120 × 8	14 × 2	14 × 3
6	15582981−2310077	26928384	50799	120 × 8	14 × 3	14 × 3
7	16053215−1933159	26927872	50799	120 × 8	14 × 3	14 × 4
8	16222160−2217307	26926848	50799	120 × 10	14 × 2	14 × 2

Notes. SH spectra are all from PID 50799. 2MASS 04381486+2611399 is the only source without an LL spectrum.
[a] Exposure times are in seconds.

2011 for the same result obtained by analyzing near-infrared molecular lines). Thus, both in situ thermochemical processes and dynamical transport of icy planetesimals in the midplane may alter the composition of disk atmospheres.

Pascucci et al. (2009) have extended the study of gas disk atmospheres to very low mass stars and brown dwarfs (hereafter, BDs) using low-resolution ($R \sim 120$) *Spitzer* spectra. They report the first detections of C_2H_2 bands in BD disks and lower HCN/C_2H_2 ratios, but larger grain sizes than in T Tauri disk atmospheres. Motivated by these differences as a function of spectral type, here we analyze in detail the only high signal-to-noise ratio (S/N) spectra of very low mass star and BD disks acquired with the high-resolution mode of the *Spitzer* Infrared Spectrograph (IRS; Houck et al. 2004). The sample comprises eight objects with spectral types (SpTy) ranging from M3 to M7.5; half of them have SpTy later than ∼M6 and are treated here as BDs (see, e.g., Luhman et al. 2007 for a discussion of the hydrogen-burning mass limit for young objects). The sources are located in the ∼1 Myr-old Taurus (Kenyon et al. 2008) and ∼10 Myr-old Upper Sco (Pecaut et al. 2012) star-forming regions (see Table 1). Our sample is biased against sources with strong jets and may be slightly biased toward older objects. We report the first detections of [Ne II] and H_2 pure rotational lines toward BDs (Sections 3.1 and 3.2) and show that X-rays likely dominate over EUV in heating and ionizing the disk surface of these very low mass objects (Sections 5.1 and 5.2). We confirm the lower HCN/C_2H_2 abundance in BD disks with respect to T Tauri disks (Sections 3.2 and 4) previously reported by Pascucci et al. (2009). We also report the first detections of H_2O lines in BD disks (Section 3.2) but observe an overall depletion of water vapor in comparison to other simple organic molecules. In Sections 5.3, we discuss the possibility that the high C_2H_2/HCN and HNC/H_2O ratios reflect an enhanced carbon chemistry in the inner regions of very low mass star and BD disks.

2. OBSERVATIONS AND DATA REDUCTION

Observations were carried out with the *Spitzer* IRS Short-High (SH) module in 2009 May as part of the program PID 50799 (PI: G. Herczeg). The SH module covers the wavelength range ∼10–19 μm with a resolving power of approximately 700. Lower resolution spectra were also acquired within the same program using the Short-Low (SL: 5.2–14.5 μm) and Long-Low modules (LL: 14–38 μm) for all but three sources (objects #1, 3, and 4). For these three sources, we retrieved and reduced archival data from other programs (see Table 2). 2MASS J04381486+2611399 (object #1) is the only BD that was not observed with the LL module, hence its low-resolution spectrum extends only out to 14.5 μm. Table 2 provides the observational log.

The low-resolution spectra were reduced using the data reduction scripts developed by the "Formation and Evolution of Planetary Systems" Spitzer Legacy team (Meyer et al. 2006). We refer to Bouwman et al. (2008) for details about the data reduction. These spectra are primarily used to verify the flux calibration and spectral shape of the high-resolution spectra. They are also used, in combination with published photometry, to characterize the spectral energy distributions (SEDs) of our eight sources (see Figure 1). In what follows, we focus on describing the observational strategy and reduction of the high-resolution data.

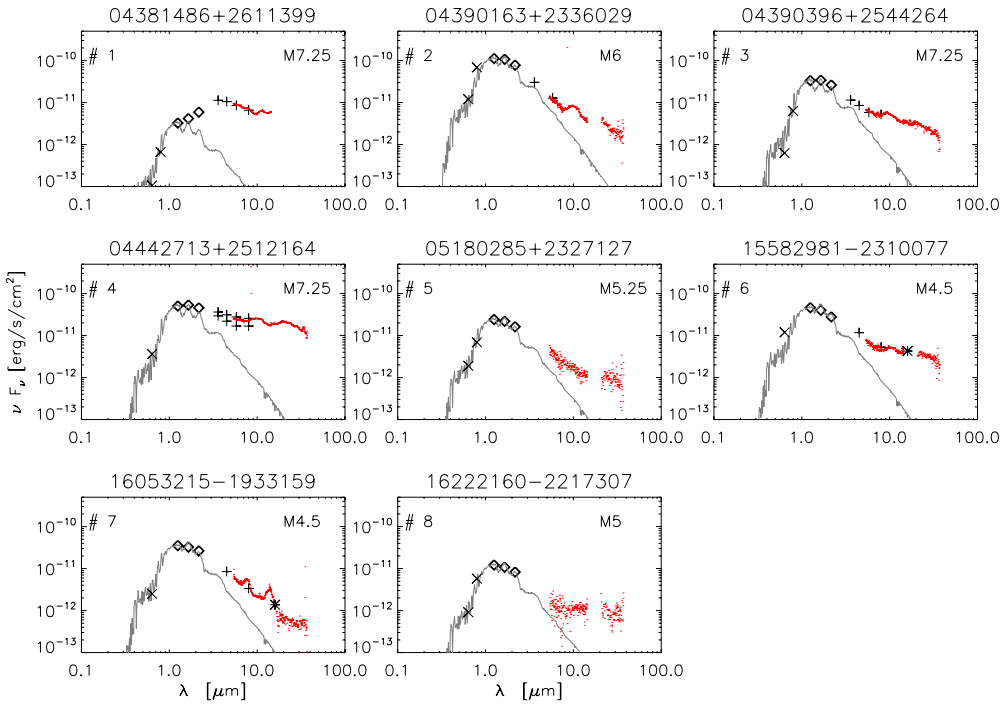

Figure 1. Spectral energy distributions of our targets. We plot *R* and *I* (X), 2MASS *J*, *H*, and *K* (diamonds), IRAC 3.6, 4.5, 5.8, and 8 μm (+), and MIPS 24 μm (asterisk) fluxes. Low-resolution *Spitzer*/IRS spectra are shown with dot red symbols. NEXTGEN model atmospheres are plotted with gray lines. Objects #1 and 4 have the largest infrared excess among our targets.

(A color version of this figure is available in the online journal.)

Targets were acquired with the visual Pointing Calibration and Reference Sensor and placed on two positions along the slit (at one-third and two-thirds of the slit length), following the standard IRS staring mode technique. Sky exposures were obtained right after the on-source exposures at 60″ north and south of each target. These exposures are used to remove the infrared background emission and to reduce the number of *rogue* pixels. The data reduction was carried out with *IDL* custom routines, following the steps outlined in Pascucci et al. (2006) and the implementations on the noise statistics and bad pixels identification developed by Carr & Najita (2011). After image combination, background subtraction, and pixel correction, we extracted one-dimensional spectra with the full aperture extraction routine in SMART (Higdon et al. 2004). We processed 10 high S/N spectra of the calibrator ξ Dra, all in the same way, to create one-dimensional spectral response functions (for each order and at each nod position) from the known stellar model atmosphere.[5] We divided the source spectra by the spectral response functions and combined spectral orders using appropriate weighting in the overlapping regions. Finally, to estimate the noise in the average spectra, we averaged the flux-calibrated spectra at the two nod positions and divided their absolute difference by two.

The reduced SH spectra are shown in Figure 2. For all objects except #4, the high-resolution spectra match in flux and shape with the low-resolution spectra, within the 10% photometric accuracy of the IRS high-resolution mode. The low-resolution spectrum of object #4 is, overall, ∼20% higher than the high-resolution spectrum. Because the low- and high-resolution spectra are not contemporaneous (see Table 2), and source #4 showed a ∼30% change in its *Spitzer*/IRAC fluxes

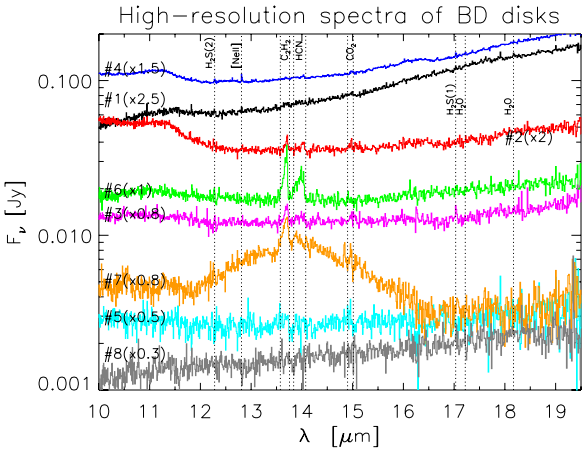

Figure 2. High-resolution *Spitzer* spectra of our targets. Bands and emission lines discussed in the text are marked with dotted lines. Spectra have been scaled by the factor in parenthesis to better separate them. The broad emission between 12 and 16 μm in object #7 is further discussed in the Appendix.

(A color version of this figure is available in the online journal.)

in one year (Figure 1 and Luhman et al. 2010), we attribute the difference between the high- and low-resolution spectra to intrinsic source variability.

3. OBSERVED INFRARED LINES

Before presenting the atomic and molecular lines detected in our sample, we compute additional stellar (BD) parameters that will be useful in interpreting the observations. We also briefly discuss the SEDs of our very low mass stars and BDs.

Table 1 provides literature SpTy, distances, masses, and bolometric luminosities for all our sources. Mass accretion rates ($M_{\rm acc}$) are available for four sources while three sources have

[5] http://irsa.ipac.caltech.edu/data/SPITZER/docs/irs/calibrationfiles/decinmodels/

Table 3
Estimated Stellar and Brown Dwarf Properties

ID	2MASS J	Log(M_{acc}) ($M_\odot$ yr^{-1})	Log(L_X) (erg s^{-1})	Log(L_{FUV}) ($L_\odot$)
1	04381486+2611399	[a]	28.2	−4.86
2	04390163+2336029	−9.8	28.3	[a]
3	04390396+2544264	[a]	28.0	−5.81
4	04442713+2512164	−11.0	[a]	[a]
5	05180285+2327127	−9.3	28.5	[a]
6	15582981−2310077	[a]	28.8	−3.67
7	16053215−1933159	[a]	28.8	−3.59
8	16222160−2217307	...	28.5	...

Note. [a] See Table 1 for values reported in the literature

Table 4
Line Fluxes and 3σ Upper Limits for [Ne II] and H_2 Transitions

ID	2MASS J	[Ne II]	H_2 $S(2)$	H_2 $S(1)$
1	04381486+2611399	8.5 ± 1.9	<10	5.6 ± 2.5
2	04390163+2336029	4.3 ± 1.9	<15	<6
3	04390396+2544264	<9	10 ± 3	8.5 ± 3.5
4	04442713+2512164	22.6 ± 2.5	13 ± 3	13 ± 4
5	05180285+2327127	<7	<12	<6
6	15582981−2310077	<7	13 ± 4	<10
7	16053215−1933159	<5	<10	<6
8	16222160−2217307	<7	<6	<9

Note. Fluxes are in units of 10^{-16} erg s^{-1} cm^{-2}.

far-UV (FUV) luminosities (L_{FUV}) from the literature (see Table 1). Object #8 (16222160-2217307) is the only one for which there are no M_{acc} or L_{FUV} estimates. Sources with L_{FUV} are from the FUV atlas of Yang et al. (2012); they also have accretion luminosities (L_{acc}) reported in the same paper. For these three sources, we compute M_{acc} using the standard relationship with L_{acc} (e.g., Equation (8) in Gullbring et al. 1998), fixing the disk inner radius to five times the stellar radius. The stellar radius is computed using the Stefan-Boltzmann relation with the bolometric luminosity given in Table 1, the stellar effective temperature from the source SpTy (also in Table 1), and the temperature scale of Luhman et al. (2003). M_{acc} calculated this way are reported in Table 3. For the four sources with literature M_{acc}, we use the relationship mentioned above to compute L_{acc} and then convert L_{acc} into L_{FUV} following Yang et al. (2012). L_{FUV} computed this way are reported in Table 3. Finally, only BD #4 has a measured X-ray luminosity (see Table 1). We estimate L_X for all other sources using the empirical relation between X-ray luminosity and stellar mass found by Güdel et al. (2007) and list the estimated L_X in Table 3.

The SEDs of our very low mass stars and BDs are shown in Figure 1. They include optical and infrared photometry (*R*, *I*, *J*, *H*, *K*, *Spitzer*/IRAC, and MIPS) and our low-resolution *Spitzer*/IRS spectra. We also show the NEXTGEN (Hauschildt et al. 1999) model atmosphere (scaled to the source *J*-band flux) appropriate to each source (using the SpTy in Table 1 and temperature scale in Luhman et al. 2003). Six out of eight sources have moderate infrared excess emission, with observed fluxes at 8 μm that are three to seven times the photospheric fluxes. BDs #1 and #4 have fluxes that are more than an order of magnitude larger than their photospheric fluxes. BD #1 is also the least luminous at optical wavelengths, in agreement with being surrounded by an almost edge-on disk (Luhman et al. 2007). The IRS low-resolution spectrum of object #7 shows two prominent broad bands between 7–8 and 12–16 μm (Figure 1) that appear to be emission features. The feature at longer wavelengths is also clearly seen in the high-resolution spectrum (Figure 2). These bands are not spatially extended beyond the relatively narrow slit of the low-resolution spectrograph (~500 AU projected width), hence must be associated with the star/disk system. In the Appendix, we speculate on the possible origin of these features.

3.1. Atomic/Ionic Lines

The strongest atomic/ionic lines detected in *Spitzer* spectra of T Tauri disks are the H I (7–6) at 12.37 μm and the [Ne II] at 12.81 μm (e.g., Pascucci et al. 2007; Lahuis et al. 2007). We have searched for these emission lines in our sample and report the first [Ne II] detections toward BD disks (see Figure 3).

To estimate line fluxes and upper limits, we followed the procedure outlined in Pascucci et al. (2007). In brief, when a [Ne II] line is detected, we fit a Gaussian plus a first-order polynomial to the spectral region within ±0.05 μm of the line (10 pixels). In the case of nondetections, we fit the same wavelength region with a first-order polynomial and compute a 3σ upper limit from the rms of the continuum-subtracted spectrum. The 1σ uncertainties on detected lines are also computed from the rms of continuum-subtracted spectra in a region just outside the line. Our results are summarized in Table 4. The brightest [Ne II] emission is from BD #4 with a line flux of ~23×10^{-16} erg s^{-1} cm^{-2}. Line fluxes from BD #1 and #2 are ~3 and five times weaker, respectively. We also note that the emission toward source #2 is only a tentative detection (slightly above 2σ) and should be confirmed via future observations with *James Webb Space Telescope* (*JWST*). For the other five targets, we estimate 3σ upper limits in the [Ne II] line that range between (4–9) × 10^{-16} erg s^{-1} cm^{-2}. Similar upper limits are found for the H I(7–6) line, which is never detected in our sample. We will discuss in Section 5.1 the likely origin of the [Ne II] emission toward very low mass stars and BDs.

3.2. Molecular Transitions

The *Spitzer* IRS SH module covers many rotational transitions from H_2O and OH, as well as rovibrational bands from simple molecules such as C_2H_2, HCN, and CO_2 (Q-branches at 13.7, 14.0, and 14.97 μm, respectively). These molecules are frequently detected toward T Tauri stars with disks and likely trace the warm disk atmosphere (e.g., Pontoppidan et al. 2010). The H_2 infrared lines have been also detected toward T Tauri disks (Lahuis et al. 2007; Carr & Najita 2011), though some detections may be tracing outflows or cloud emission rather than the disk itself (Lahuis et al. 2007).

Here, we report the first detections of H_2 pure rotational lines toward BD disks (see Figure 4). The procedure to measure line fluxes and upper limits is identical to that used for the [Ne II] lines (Section 3.1 and Table 4). Firm H_2 detections ($\geqslant 3\sigma$) are only available for sources #3, 4, and 6 in the H_2 $S(2)$ at 12.28 μm and for source #4 in the H_2 $S(1)$ at 17.03 μm. Tentative detections (above 2σ) are also reported for #1 and 3 in the H_2 $S(1)$ transition (see Figure 4 and Table 4). Object #4 is the only one where both H_2 transitions are firmly detected and point to similar line fluxes. When lines are not detected, 3σ upper limits are found to be ~(4–10) × 10^{-16} erg s^{-1} cm^{-2}. We will further discuss these detections and upper limits in Section 5.2.

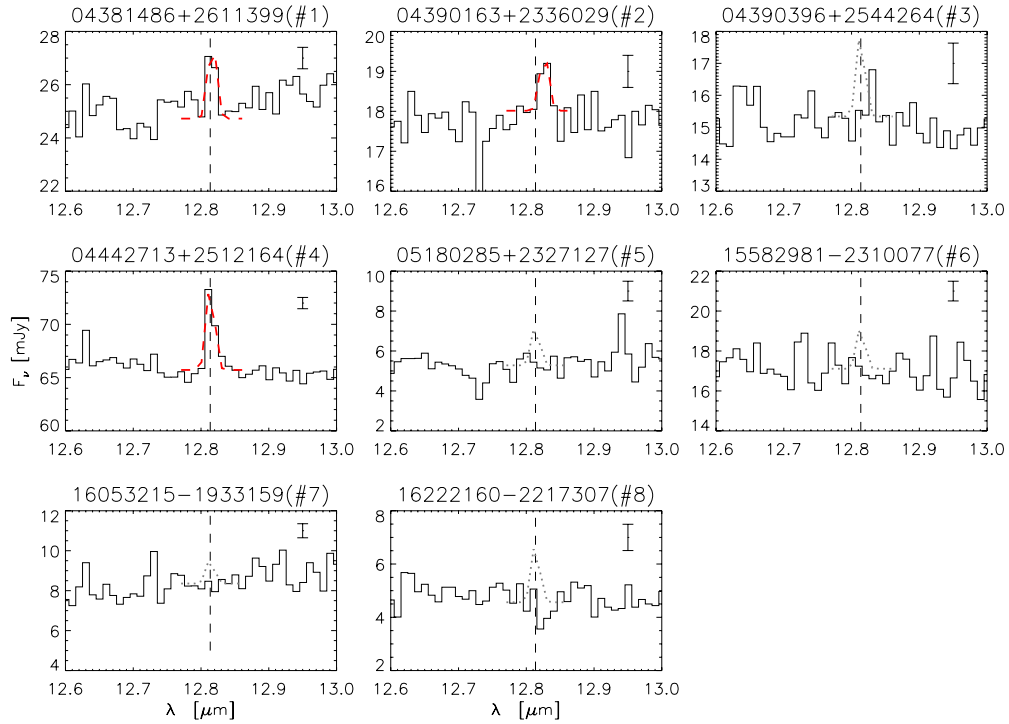

Figure 3. Expanded view of the wavelength region around the [Ne II] line. On top of the continuum emission, we overplot the best Gaussian fits to the data (red dashed lines) or, in the case of nondetections, the hypothetical 3σ upper limits (gray dotted lines). The errorbar provides the 1σ uncertainty based on the rms on continuum-subtracted spectra (see the text).

(A color version of this figure is available in the online journal.)

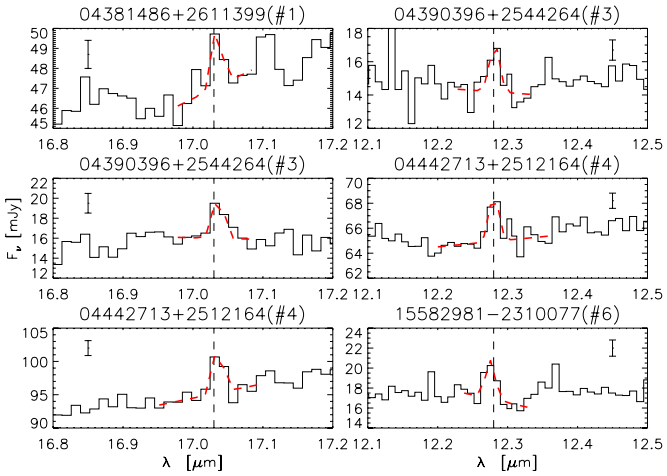

Figure 4. Expanded view of the wavelength region around the H_2 lines. We only show spectra where either the H_2 $S(2)$ at 12.28 μm or the $S(1)$ line at 17.03 μm have been detected. On top of the continuum emission, we overplot the best Gaussian fits to the data (red dashed lines). The emission around 17.1 μm toward 2MASS J04381486+2611399 (#1) may be from H_2O (see Figure 5). The errorbar provides the 1σ uncertainty based on the rms on continuum-subtracted spectra (see the text).

(A color version of this figure is available in the online journal.)

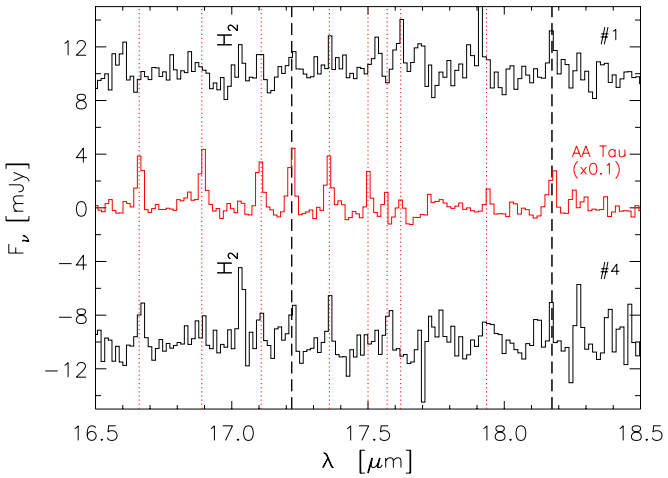

Figure 5. Continuum-subtracted spectra (black lines) of the two BDs toward which we have tentative detections of water lines. The continuum-subtracted spectrum of the T Tauri star AA Tau (Carr & Najita 2008) is plotted in the middle of the figure in red. A constant shift has been applied to BD spectra while the spectrum of AA Tau has been scaled by the factor in parenthesis to facilitate the comparison with the BD spectra. Black vertical dashed lines mark the 17.22 and 18.17 μm H_2O transitions for which we report fluxes or upper limits in Table 5. Red vertical dotted lines mark other water transitions that are detected in AA Tau.

(A color version of this figure is available in the online journal.)

We also report detections of the C_2H_2 and HCN rovibrational bands toward objects #2, 3, 6, and 7 (see later the continuum-subtracted spectra in Figure 8—the latter HCN detection is very weak). In all objects, the C_2H_2 band emission appears stronger than the HCN emission. This pattern was already recognized in low-resolution *Spitzer* spectra from 19 very low mass stars and BDs belonging to the Cha I star-forming region (Pascucci et al. 2009) and is opposite to what is seen in T Tauri disks (Pascucci et al. 2009; Carr & Najita 2011). The five-times-higher resolution of the spectra presented here enables us to detect fainter emission and model the shape of the band emission (see Section 4). We also present the first CO_2 detections toward BD disks (objects #2, 3, and 7) and tentative detections of H_2O lines in the spectra of objects #1 and #4 (see Figure 5). We do not have any detection of OH lines in our spectra.

Table 5
Line Fluxes and 3σ Upper Limits for Organic Molecules and Water Lines

ID	2MASS J	C_2H_2	HCN	CO_2	H_2O (17.22 μm)	H_2O (18.17 μm)
1	04381486+2611399	<32	<31	<18	5 ± 2	6 ± 2
2	04390163+2336029	33.8 ± 9	36.2 ± 9	14.5 ± 5	<12	<7
3	04390396+2544264	56.0 ± 11	44.5 ± 10	9.6 ± 4	<9	<17
4	04442713+2512164	<23[a]	<38[a]	<24	8 ± 3	<6
5	05180285+2327127	<25	<24	<12	<7	<7
6	15582981−2310077	205 ± 14	169 ± 13	<21	<8	<19
7	16053215−1933159	106 ± 11	37.6 ± 11	11.1 ± 4.8	<4	<7
8	16222160−2217307	<21	<20	<14	<6	<5

Notes. Fluxes are in units of 10^{-16} erg s^{-1} cm^{-2}. Integrations are performed over the following wavelength ranges: C_2H_2 (13.576–13.756 μm); HCN (13.837–14.075 μm); CO_2 (14.900–15.014 μm); H_2O (17.19–17.25 μm and 18.12–18.22 μm). 3σ upper limits are computed for an unresolved line for the H_2O rotational line, over two times the resolution for CO_2, and over three times the resolution for C_2H_2 and HCN. This choice reflects the width of the rotational and rovibrational lines when detected.
[a] HCN and to less extent C_2H_2 emission are clearly contaminated by water lines.

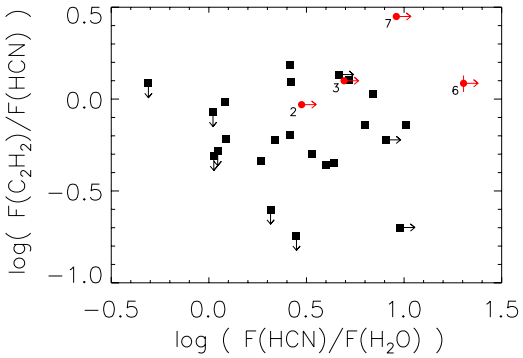

Figure 6. Log–log plot of molecular flux ratios (see also Table 5). For comparison with other studies, we use the H_2O transition at 17.22 μm. Red circles are very low mass star and BD disks from this study. Black squares are T Tauri disks from Pontoppidan et al. (2010) and Salyk et al. (2011). Our sample occupies the upper right portion of the plot: C_2H_2 fluxes $\geqslant$ HCN fluxes and HCN fluxes more than $\sim$3 times the H_2O fluxes at 17.22 μm.
(A color version of this figure is available in the online journal.)

To quantify the strength of the molecular emission, we measure fluxes in the H_2O 17.22 and 18.17 μm lines[6] and in the organic molecular bands using a procedure similar to that outlined in Salyk et al. (2011). First, we fit a linear continuum using pixels shortward and longward of the emission. Then, we subtract the continuum emission and integrate the flux within wavelength regions that cover the full emission (see Note to Table 5). Line flux upper limits are calculated from the rms in the continuum-subtracted spectra using line widths appropriate to each transition: an unresolved line width for the H_2O rotational transitions, three times the resolution for the C_2H_2 and HCN bands, and two times the resolution for the CO_2 band. The 1σ uncertainties on detected lines are also calculated from the rms in the continuum-subtracted spectra. Table 5 reports our line flux measurements and 3σ upper limits when lines are not detected. The strongest band emission is typically from C_2H_2, followed by HCN and by CO_2. Water lines are the weakest and tentatively detected at the 2σ–3σ level only toward the two sources with no emission from organic molecules (objects #1 and #4). These tentative detections should be prime candidates for followup observations with *JWST*. Figure 6 compares molecular line flux ratios from our sample with those from T Tauri disks (Pontoppidan et al. 2010; Salyk et al. 2011). While there is some overlap between the two samples, very low mass star and BD disks tend to occupy the upper right corner of the plot. The data in Figure 6 confirm the result from Pascucci et al. (2009) that BD disks have larger C_2H_2/HCN flux ratios than the average T Tauri disk. In addition, it shows that the HCN/H_2O (and C_2H_2/H_2O) flux ratios tend to be larger in BD than in T Tauri disks. We will further discuss the significance of this result in Section 5.3.

[6] We do not have any detection above 3σ in the 15.17 μm H_2O line, which is often detected in T Tauri disks (see Pontoppidan et al. 2010), therefore we do not include it in our discussion.

4. LTE MODELING OF H_2O AND ORGANIC MOLECULES

Water and OH are commonly detected in the IR spectra of T Tauri stars and their many transitions can contaminate emission lines/bands from other molecules (see, e.g., Carr & Najita 2008). This is not the case for our sample, where weak H_2O lines are tentatively detected in only two BD spectra (objects #1 and 4) that do not present emission from other organic molecules (see Table 5 and Figure 5). Hence, when modeling the emission bands of organic molecules from objects #2, 3, 6, and 7, we can safely ignore any contamination from water. However, we still model the water emission to derive H_2O column density upper limits based on the line flux upper limits reported in Table 5.

We compute synthetic spectra of H_2O and organic molecules adopting a plane-parallel slab model of gas with a single temperature and column density. Molecular parameters are taken from the HITRAN 2008 database (Rothman et al. 2009). We assume the gas to be in LTE and account for optical depth effects as in Banzatti et al. (2012). Previous studies have shown that the LTE assumption can reproduce, relatively well, the line luminosities of most H_2O lines detected in T Tauri disks; only the higher energy level transitions hint at a possible departure from LTE (Carr & Najita 2011; Salyk et al. 2011). However, see Meijerink et al. (2009) for the importance of non-LTE effects in estimating column densities, especially in the case of H_2O, whose mid-infrared transitions span four orders of magnitudes in critical density ($\sim 10^8$–10^{12} cm^{-3}). In our simple LTE model, there are four input parameters to produce a synthetic spectrum: the gas temperature (T), the line-of-sight column density (N), the radius (R) of the projected emitting area, and the local line width. To allow a direct comparison with models of T Tauri and Herbig Ae/Be disks, we use as local line width that due only to thermal broadening, which is temperature- and molecule-dependent.

To compare the observed and synthetic spectra of C_2H_2, HCN, and CO_2, we first estimate the continuum level in

Table 6
Modeling Results

ID	2MASS J	T (K)	R (AU)	$N_{C_2H_2}$ (10^{16} cm^{-2})	N_{HCN} (10^{16} cm^{-2})	N_{CO_2} (10^{16} cm^{-2})	N_{H_2O}[b] (10^{16} cm^{-2})
2	04390163+2336029	240	0.29	15.8	18.1	9.5	< (1[+9],5)
3	04390396+2544264	240	0.26	50.1	11.7	5.6	< (1[+9],21)
6	15582981−2310077	960	0.09	12.6	8.4	<1	< (65,2[+4])
7	16053215−1933159[a]	960	0.09	4.5	1.1	0.9	< (11,333)

Notes. For all sources except source #7, T, R, and $N_{C_2H_2}$ are best-fit values from modeling the C_2H_2 band. N_{HCN}, N_{CO_2}, and the first entry of N_{H_2O} are computed by fixing T and R to those found via the C_2H_2 modeling. The second entry of N_{H_2O} is obtained using the same R as above but assuming a temperature of 600 K.

[a] For this source we cannot find a good fit to the C_2H_2 band; the emission is too broad. We have thus fixed the temperature and emitting area to those of source #6 and varied the column density to reproduce the observed flux integrated over the emission bands and lines.

[b] We used the 3σ upper limits to the 17.22 and 18.17 μm H_2O lines reported in Table 5 and give here the most stringent constraint on the column density. The first entry is for the gas temperature listed in column three of this table while the second entry is for $T = 600$ K. Values in square brackets of the form [+b] stand for 10^{+b}. Note that the water column density for objects #2 and 3 is essentially unconstrained for the low temperature case ($T = 240$ K).

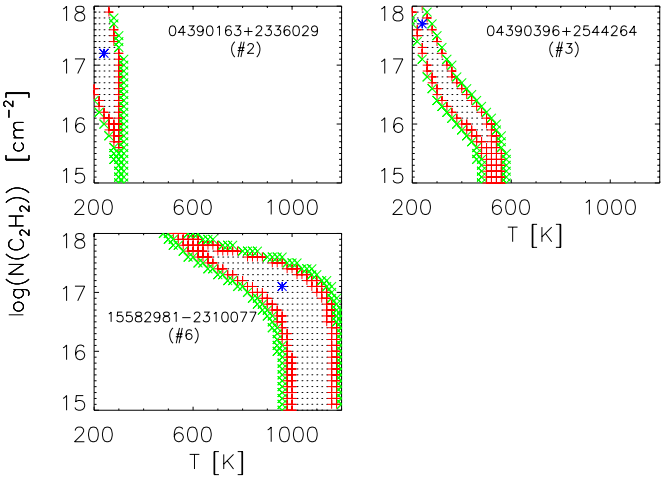

Figure 7. Plots of χ^2 as a function of temperature (T) and column density (N) for fits to the C_2H_2 Q-branch band emission. A blue asterisk marks the best-fit values (minimum χ^2). Black dots, red crosses, and green X's mark the regions within 1σ, 2σ, and 3σ, respectively when assuming a Gaussian χ^2 distribution. (A color version of this figure is available in the online journal.)

three wavelength regions: two outside and one in between the emission bands. We find that second-order polynomials can reproduce well the continuum, except for object #7, where the broad emission between 14 and 16 μm is best modeled with a fourth-order polynomial. Next, we subtract the continuum emission and use the LTE model described above to reproduce the continuum-subtracted band emission from each molecule. Because the C_2H_2 rovibrational band is typically the strongest, we first run a grid of models with temperatures varying between 50 and 1200 K (in steps of 20 K) and column densities between 10^{14} and 10^{18} cm^{-2} (in logarithmic steps of 0.1) to reproduce its profile. The radius of the projected emitting area is varied to match the integrated area below the emission band, but it is kept smaller than 1 AU. In other words, solutions with emitting radii extending beyond 1 AU are not considered plausible, given the extension of the mid-infrared region in BD disks, and thus are discarded. We compute χ^2 from the difference of the model and observed spectrum for each grid point to estimate the best-fit values and confidence intervals. Our results are summarized in Table 6 and Figure 7. Only for source #7 could we not find good fits within the explored parameter range; its C_2H_2 band emission appears to be too broad even for the highest temperature in our grid (1200 K). There is also some extra emission around 13.85 μm, which is not seen toward other sources, and may be due to contamination from other molecules not considered in our model. For this source, we assume the same gas temperature and emitting radius as for source #6, and compute the $N_{C_2H_2}$ that reproduces the observed flux integrated over the band.

Figure 7 shows the χ^2 as a function of the gas temperature, T, and column density, $N_{C_2H_2}$, for our fits to the C_2H_2 Q-branch band emission of sources #2, 3, and 6. With the assumption that the χ^2 distribution is Gaussian, we also draw the 1σ, 2σ, and 3σ confidence intervals. This figure is instructive because it shows that there is a relatively large range of plausible T and $N_{C_2H_2}$ (even within 1σ), and that these two input parameters are degenerate (higher T is offset by lower N). This same behavior has been noted in previous studies of T Tauri disks (Carr & Najita 2011; Salyk et al. 2011). If we consider the 1σ intervals, we see that the gas disk temperature of the Taurus BD #2 can be as low as 200 K and up to 280 K, with $N_{C_2H_2}$ varying between 10^{16-18} cm^{-2}. The gas temperature of BD #3, also in Taurus, can be as high as 500 K; column densities can be as low as 5×10^{15} cm^{-2} for these higher T. The disk surfaces of objects #6 and #7, which are in Upper Sco, are definitively hotter than that of the Taurus BDs #2 and 3. Within the 1σ interval, T varies between 660 and 1140 K, and $N_{C_2H_2}$ between 1–500 $\times$ 10^{15} cm^{-2}, for object #6. While the average bolometric and X-ray luminosities of #6 and 7 are only about a factor of 3 higher than the average values for BDs #2 and 3, their average FUV luminosity is more than a factor of 50 higher (see Tables 1 and 3). The overall higher heating may be responsible for the hotter disk surface of #6 and 7 we infer from our fits to the C_2H_2 rovibrational bands (see also Section 5.3). We note that at temperatures as high as ~1000 K, polycyclic aromatic hydrocarbons (PAHs) and C_2H_2 can be closely related, and the destruction of PAHs may enhance the abundance of C_2H_2 (Frenklach & Feigelson 1989; Morgan et al. 1991; Kress et al. 2010).

Our approach shows that there are large uncertainties in determining the gas properties of even the strongest rovibrational bands: those from C_2H_2. Therefore we do not attempt to independently determine the gas properties for HCN, CO_2, and H_2O, but rather assume the same temperature and emitting area as that found for C_2H_2. We then scale the column densities to match

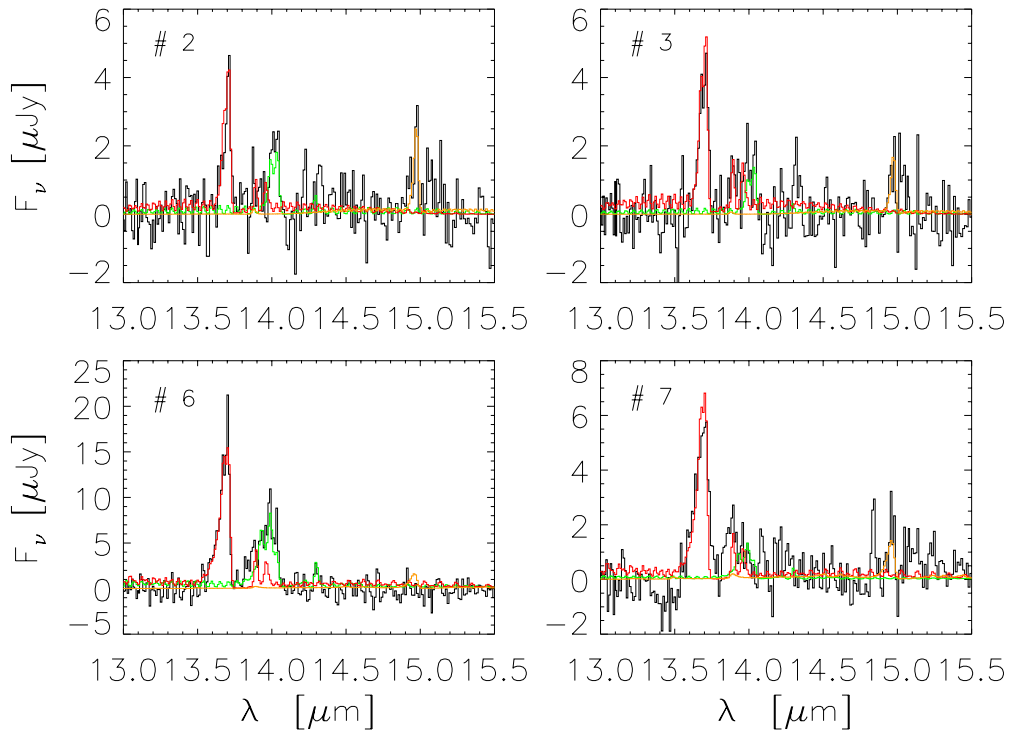

Figure 8. Continuum-subtracted spectra (black lines) of the four very low mass stars and BDs where we detect molecular rovibrational emission bands. Best-fit synthetic spectra of C_2H_2 (red histogram), HCN (green histogram), and CO_2 (orange histogram) are overplotted on the data. The best-fit parameters are summarized in Table 6.

(A color version of this figure is available in the online journal.)

the integrated flux (or 3σ upper limits) over the other molecular bands. In the case of HCN, we first subtract the best-fit C_2H_2 model spectrum reported in Table 6 and recompute the HCN line flux. Best-fit parameters are reported in Table 6 and the resulting synthetic spectra are shown in Figure 8. For water, we report column density upper limits for two temperatures: (1) the temperature obtained from the best fit to the C_2H_2 band (third column in Table 6) and (2) the temperature of 600 K that is found to be typical of the water-emitting layer of T Tauri disks (Carr & Najita 2011). The emitting radius is always fixed to that found from the best fit to the C_2H_2 band (fourth column in Table 6). The column density of water is poorly limited by our data and very sensitive to the assumed temperature. In particular, if water vapor is as cold as C_2H_2 in objects #2 and 3, our line flux upper limits are not stringent enough to place any useful bounds on the amount of water on the surface of these disks. This is because, in offsetting the low flux due to the cold gas, water lines become optically thick and grow very slowly with increasing column density. As an example, for $T_{H_2O} = 240$ K and $N_{H_2O} = 10^{20}$ cm^{-2}, the 17.22 μm feature is the brightest of the water lines but has an optical depth at the line center of $\sim$50. Such cold water emission is not typical of T Tauri disks (Carr & Najita 2011; Salyk et al. 2011). However, lacking limits from disks around lower mass stars, we include the results from this extreme temperature in our discussion.

5. DISCUSSION

5.1. On the Origin of the [Ne II] Emission toward BD Disks

Ground-based observations have spectrally resolved the brightest [Ne II] lines detected with *Spitzer* toward T Tauri stars (Herczeg et al. 2007; van Boekel et al. 2009; Najita et al. 2009; Pascucci & Sterzik 2009; Pascucci et al. 2011; Sacco et al. 2012; Baldovin-Saavedra et al. 2012). These data have demonstrated that [Ne II] emission can trace either (1) jets and outflows far from the star (typically toward high-accreting stars) or (2) the hot ($\sim$10,000–5000 K) disk surface ionized by stellar EUV and/or X-ray photons (in moderate- to low-accreting stars, $M_{acc} \lesssim 10^{-8}\ M_\odot$ yr^{-1}). When disk emission is detected, most [Ne II] lines are blueshifted by a few km s^{-1} with respect to the stellar velocity, pointing to unbound gas in a photoevaporative thermal wind (e.g., Pascucci & Sterzik 2009; Sacco et al. 2012). It is debated whether [Ne II] emission traces either the fully ionized EUV or the partially ionized X-ray disk layer, hence mass loss rates via photoevaporation are yet unconstrained (e.g., the recent review by Alexander et al. 2013).

To decide whether our [Ne II] detections trace jets/outflows or the BD disk surface, we plot the [Ne II] luminosity ($L_{Ne\,II}$) as a function of the stellar mass accretion rate (M_{acc}). Together with our sample, we include all other *Spitzer* detections and upper limits reported in the literature for T Tauri stars (see Figure 9). The complete [Ne II] sample spans almost six orders of magnitude in M_{acc} and three orders of magnitude in $L_{Ne\,II}$. When we extrapolate the $L_{Ne\,II}$–M_{acc} relation found for T Tauri stars with known jets (Güdel et al. 2010) to the BD regime, we see that only the strongest of our [Ne II] detections (from source #4) can be attributed to jets or outflows. Indeed, Bouy et al. (2008) detected strong forbidden optical lines (O I, S II, and N II) in the high-resolution spectrum of source #4 (2MASS J04442713+2512164), suggesting that this object is undergoing significant mass loss via a jet or outflow. We conclude that most of the [Ne II] emission from source #4 is not associated with the disk but produced in circumstellar material shocked by jets or outflows.

BDs #1 and 2 have lower $L_{Ne\,II}$ than source #4, by factors of $\sim$3 and 5, respectively (the detection toward #2 is only tentative).

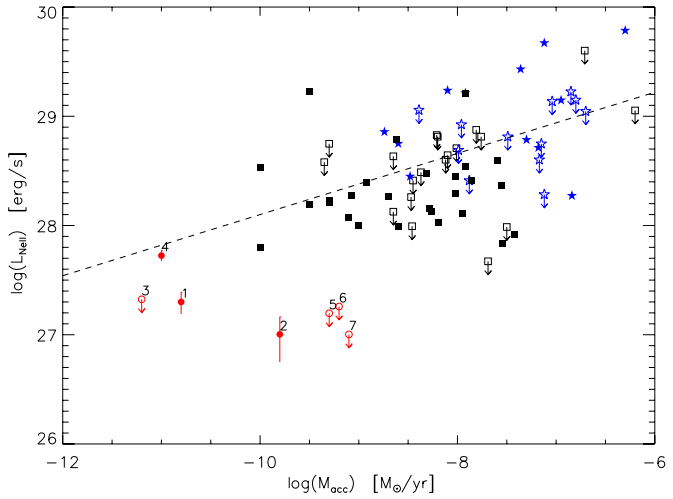

Figure 9. [Ne II] line luminosities vs. mass accretion rates. Brown dwarf disks from this work are represented with red circles. Black squares refer to T Tauri disks (including transition disks) without jets, and blue stars to jet sources from the literature (Güdel et al. 2010; Baldovin-Saavedra et al. 2012; Espaillat et al. 2013). Filled and open symbols are used for detections and nondetections, respectively. Our object #8 does not have a measured mass accretion rate, hence it is not included in the figure.

(A color version of this figure is available in the online journal.)

It is interesting to speculate what X-ray or EUV fluxes are needed to reproduce these lower luminosities, assuming that the [Ne II] emission originates entirely in the ionized surface of BD disks. In the simplest scenario in which neon atoms are ionized solely by stellar EUV photons, we can convert the observed [Ne II] luminosities into the rate of ionizing photons reaching the disk surface ($\Phi_{\rm EUV}$, Hollenbach & Gorti 2009, HG09). The [Ne II] detections from #1 and 2 correspond to $\Phi_{\rm EUV}$ of 0.6–1.2 $\times$ 10^{40} s^{-1}. These values are ∼5–10 times lower than the $\Phi_{\rm EUV}$ inferred for T Tauri stars (Alexander et al. 2005; Pascucci et al. 2012) and represent upper limits to the EUV luminosities impinging on the disk surface. This is because part, or most of, the [Ne II] emission could arise from a disk layer ionized by stellar X-rays (see below). It is unclear whether EUV photons are from the stellar chromosphere and/or accretion processes (see, e.g., Alexander et al. 2005). If the latter dominate, then $\Phi_{\rm EUV}$ should scale with the accretion luminosity or, equivalently, with the stellar FUV luminosity ($L_{\rm FUV}$), since the two quantities are tightly correlated (Yang et al. 2012). $L_{\rm FUV}$ for T Tauri stars cluster between 0.001–0.01 $L_\odot$ (see Figure 12 in Yang et al. 2012) while the $L_{\rm FUV}$ we estimate for our sample are ∼10–1000 times lower (see Tables 1 and 3). X-ray luminosities ($L_{\rm X}$) decrease with stellar mass less steeply than $L_{\rm FUV}$. The $L_{\rm X}$ of our sources (most of which are estimated from the source mass—see Table 3) are ∼10–100 times lower than the average $L_{\rm X}$ of T Tauri stars (∼10^{30} erg s^{-1}; Güdel et al. 2007). These trends suggest that X-rays, rather than EUV photons, are the main ionizing source of neon atoms in BD disk atmospheres. According to the models of Schisano et al. (2010), unscreened X-ray luminosities of $\sim 5 \times 10^{28}$ erg s^{-1} are necessary to produce $L_{\rm Ne\,II} \sim 10^{27}$ erg s^{-1}, which is close to our [Ne II] fluxes and 3σ upper limits. Therefore, the fact that the majority of our disks remain undetected in the [Ne II] line is consistent with their low X-ray luminosities. In summary, a disk origin is plausible for the [Ne II] emission reported toward BDs #1 and 2, and X-ray ionization is likely the major contributor to neon ions in their disk atmosphere.

The detection of [Ne II] emission from BD disk atmospheres shows that even young very-low-mass objects have enough high-energy photons to create a fully or partially ionized hot surface. Whether this surface is unbound and part of a photoevaporative flow, as in moderate- to low-accreting T Tauri stars, cannot be tested with the IRS low resolving power. A resolution of ∼10 km s^{-1} is needed to spectrally resolve lines tracing the flow and detect the few km s^{-1} blueshifts in peak centroid with respect to photospheric lines. Due to the faintness of our sample, and BD disks in general, this test will have to wait for high-resolution spectrographs mounted on 40-m-class telescopes.

5.2. Warm Gas Masses from H_2 Detections

H_2 pure rotational lines are found to be relatively weak toward T Tauri stars with respect to emission from other molecules and from atoms or ions. The *Spitzer* "Cores to Disks" legacy program reports that only 6 out of 76 young (∼Myr-old) disks present the H_2 $S(2)$ line in their mid-infrared spectra (Lahuis et al. 2007). The H_2 $S(1)$ line is detected in only 1 out of 76 spectra. Because of the large beam of *Spitzer* and the lack of "sky" observations for this program, extended (envelope, local cloud, jet) emission can potentially contaminate some of the reported line fluxes (Lahuis et al. 2007). Deeper observations and a better sky subtraction increase the H_2 detection rate. Carr & Najita (2011) identify the H_2 $S(1)$ transition toward 6 out of their 11 Taurus T Tauri stars but do not provide H_2 $S(2)$ fluxes because of contamination from much stronger H_2O and OH lines around 12.28 μm. Our observing technique and data reduction are similar to theirs. In addition, our sample exhibits weaker water and OH emission than T Tauri disks (see Section 3.2) resulting in an H_2 detection rate similar to that reported by Carr & Najita (2011), even toward sources that are about an order of magnitude fainter in the continuum.

Similarly to the continuum emission, our H_2 fluxes are about an order of magnitude lower than those observed toward T Tauri disks (Carr & Najita 2011) and predicted from disks irradiated by FUV and X-ray photons from T Tauri stars (Nomura et al. 2007). This is in line with the lower FUV and X-ray luminosity of very low mass stars and BDs, and suggests that our H_2 lines are indeed tracing disk gas. In the assumption that this gas is in LTE and the lines are optically thin,[7] we can use the H_2 $S(2)$ and H_2 $S(1)$ detections (or upper limits in one of the two) to compute a gas excitation temperature, $T_{\rm ex}$ (see, e.g., Thi et al. 2001 for the equations). Our measurements are consistent with $F_{\rm H_2S(1)} \sim F_{\rm H_2S(2)}$, which implies $T_{\rm ex} = 645$ K (with the assumptions outlined above). Including the 1σ uncertainties on the measured fluxes for objects #4 (Table 4) expands the range of possible $T_{\rm ex}$ to 450–1200 K. If we then use these temperatures to compute a gas mass, we find that the H_2 rotational lines trace only ~ 2–7×10^{-4} $M_{\rm J}$ (with the largest value for gas at the lowest $T_{\rm ex}$ in the range reported above). Gas masses of BD disks ($M_{\rm disk}$) have not been measured. However, the few submillimeter and millimeter detections of the continuum dust emission suggest that the $M_{\rm disk}/M_{\rm BD}$ ratio is a few percent, if the gas-to-dust-ratio is equal to the interstellar medium value of 100 (Klein et al. 2003; Scholz et al. 2006; Ricci et al. 2012). This result points to total BD disk masses of ∼$M_{\rm J}$, more than three orders of magnitude larger than what we find from the H_2 pure rotational lines. This discrepancy is not surprising since models of disks irradiated by stellar FUV and X-rays predict that H_2 pure rotational lines

[7] This is a good approximation because of the small A-values of the pure rotational transitions.

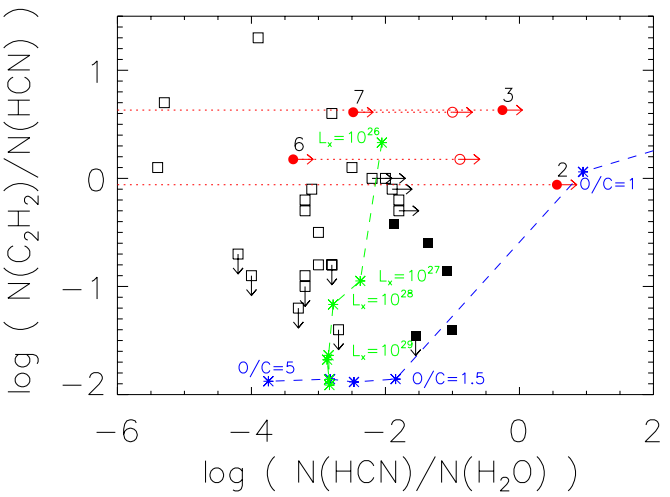

Figure 10. Column density of C_2H_2 to HCN plotted vs. that of HCN to H_2O. Red circles are brown dwarf disks from this work: filled and empty symbols are for the two closest temperatures to the $T_{C_2H_2}$ in Table 6 (400 and 600 K for #2 and 3, 600 and 960 K for #6 and 7). Emitting radii are also listed in Table 6 and are assumed the same for all molecules. Black squares are T Tauri disks from Carr & Najita (2011) while empty squares are T Tauri disks from Salyk et al. (2011). Green and blue asterisks joined by dashed lines are model predictions from Najita et al. (2011) for different L_X and O/C ratios respectively (their Tables 4 and 5). The current data hint at brown dwarf disk atmospheres having a higher carbon-to-oxygen ratio than T Tauri disk atmospheres.

(A color version of this figure is available in the online journal.)

trace mainly the warm surface of protoplanetary disks and are thus insensitive to the more abundant and cooler disk gas (e.g., Nomura et al. 2007).

The combined H_2 and [Ne II] results show that BD disks have an overall structure similar to T Tauri disks: a hot ionized layer tracing the uppermost disk atmosphere and a warm (∼600 K) molecular layer at lower vertical heights.

5.3. An Enhanced Carbon Chemistry in BD Disks?

We use the molecular column densities inferred from our LTE modeling (Section 4) to compute relative abundances of simple organic molecules and water in disks around very low mass stars and BDs. This approach complements the discussion of line flux ratios in Section 3.2 and has been previously taken for T Tauri disks (Carr & Najita 2011; Salyk et al. 2011). There are a number of caveats in using this simple approach (e.g., Carr & Najita 2011). Perhaps the most important one is that the radial and vertical regions probed by these molecules may be different, whereas they are often assumed to be the same due to the lack of spatial information with *Spitzer* observations. In addition, these infrared emission lines trace the warm disk surface, which may not be representative of the overall disk composition.

With these caveats in mind, our modeling results suggest that C_2H_2 is typically more abundant than HCN in BD disks and both C_2H_2 and HCN are more abundant than CO_2. The column density of water is very sensitive to the assumed gas temperature and useful limits on its abundance can be placed only if gas is at $T \geqslant 600$ K (even in objects #2 and 3). Figure 10 compares column density ratios of C_2H_2/HCN versus HCN/H_2O for our BD disks (red symbols) and T Tauri disks from the literature (black symbols). Horizontal red dashed lines connect the two water column densities reported in Table 6. The most obvious difference between BD and T Tauri disks is in their C_2H_2/HCN column density ratios. BD disks appear to have a systematically higher C_2H_2/HCN column density ratio: the median ratio for BD disks is ∼4 while that for the complete T Tauri sample is ∼0.6, not considering the seven C_2H_2 upper limits in the T Tauri sample. Thus, on average, C_2H_2 is about seven times more abundant than HCN in BD disks than in T Tauri disks. This difference was first pointed out from the analysis of low-resolution *Spitzer* spectra (Pascucci et al. 2009) and is corroborated by our higher resolution spectra on a different sample of BD disks. This finding is also in line with the typically higher C_2H_2/HCN strength in BD than in T Tauri disks (Section 3.2 and Figure 6). If water vapor is warm ($T \geqslant 600$ K), then Figure 10 also hints at a reduced abundance of H_2O in BD disks with respect to T Tauri disks. This possible trend is also apparent in the model-independent plot of line flux ratios, especially for the U Sco sources (Figure 6).

We now turn to theoretical models of disks irradiated by stellar FUV and X-rays (Agúndez et al. 2008; Najita et al. 2011; Walsh et al. 2012) to seek explanations for the trends in molecular abundances discussed above. We note that models report vertical column densities integrated over the height of the disk whereas observations measure line-of-sight column densities and infrared observations like ours only trace the warm disk atmosphere. So any comparison (in this as well as in other works) relies on the assumption that vertically integrated column densities are representative of the column densities in the warm disk atmosphere.

The models of Agúndez et al. (2008) are for typical T Tauri disks around Sun-like stars and include FUV heating but not X-ray heating. They find that the steady-state vertical column density of H_2O is relatively constant out to ∼3 AU from the star. On the contrary, the organic molecules HCN, C_2H_2, and CO_2 have a stronger radial dependence, with C_2H_2 (and even more CO_2) becoming less abundant in the very inner disk (inside ∼0.5 AU). At ∼1 AU, the radius likely probed with *Spitzer* around T Tauri stars, HCN is more abundant than C_2H_2 by a factor of ∼10, in agreement with inferred column density ratios for several T Tauri disks (Carr & Najita 2011; Salyk et al. 2011). Only beyond ∼2.5 AU does C_2H_2 become more abundant than HCN in the Agúndez et al. (2008) model. The models of Walsh et al. (2012) include both FUV and X-ray heating. As in Agúndez et al. (2008), they predict that H_2O is the most abundant molecule in the gas phase (after H_2) inside the snow line. However, unlike Agúndez et al. (2008), they find that HCN remains more abundant than C_2H_2 throughout the radial extent of the disk. The differences among these model results are likely due to differences in the computed gas disk temperature. Our higher C_2H_2/HCN in BD disks cannot be explained as the result of these two molecules tracing different radii in the Walsh et al. (2012) models. In the Agúndez et al. (2008) models, our result would suggest that C_2H_2 traces cooler gas, at larger radii, than HCN. This does not seem to be the case, since our T estimates from fitting the C_2H_2 band do a good job in reproducing the profile of the HCN emission band. If the predicted vertical column densities reflect atmospheric column densities, a depletion of water in BD disks (as hinted at by our line flux ratios and LTE modeling) cannot be explained as the result of radial dependencies in molecular column densities. Detailed thermochemical models of BD disks should be carried out to determine whether the different properties of BDs and their disks could explain the observed trends.

Along these lines, Najita et al. (2011) have explored how changing the properties T Tauri disks and stellar heating might affect molecular abundances. As a cautionary note, the models of Najita et al. (2011) include accretional and stellar X-ray

heating but neglect FUV heating and UV-induced processes, which generally are found to be more important than X-ray processes (Walsh et al. 2012). Najita et al. (2011) find that low accretional heating (lower disk temperature) reduces the warm molecular columns of most species but further decreases the C_2H_2/HCN ratio while keeping large column densities of H_2O. Both trends contrast with our results, suggesting that the lower accretional heating of BD disks is not responsible for the observed trends in molecular abundances. Increasing the grain size from 0.7 to 7 μm in the disk atmosphere increases the warm molecular columns of most species as well as the C_2H_2/HCN ratio. While this trend is in qualitative agreement with the observed one, 7 μm grains in the disk atmosphere enhance the C_2H_2/HCN ratio to only 0.07—still too low in comparison with the observed one. At the same time, it is very unlikely that BD disks have even larger grains in their atmosphere because many of them show 10 μm silicate emission features in their low-resolution *Spitzer* spectra (Pascucci et al. 2009). Such emission features point to the presence of dust grains with sizes $\leqslant 5$ μm. Another way of increasing the C_2H_2/HCN ratio in the models of Najita et al. (2011) is by decreasing L_X (green symbols in Figure 10). However, the C_2H_2/HCN ratios we measure for BDs are reproduced for an L_X of 10^{26} erg s^{-1}, almost two orders of magnitude lower than that in our sample (see Tables 1 and 3). A decrease in L_X should also result in a very modest change (just a factor of a few) in the HCN/H_2O ratio, with water being more abundant than HCN by a factor of $\sim$100 like in T Tauri disks. This latter trend is not consistent with our BD sample if the water-emitting layer is warm ($T \geqslant 600$ K). Even if the water nondetections alone cannot exclude a lower gas temperature, the detection of H_2 and other organic molecules show that a warm $T \sim 600$ K molecular layer is present in BD disk atmospheres. In T Tauri disk atmospheres, this layer has also a large H_2O column density inside $\sim$1 AU and produces the observed water emission spectrum (Najita et al. 2011). Hence, it is plausible that there is some warm ($T \geqslant 600$ K) water in BD disk atmospheres but perhaps not enough to be detectable in our spectra. Finally, lowering the O/C ratio from 1.5 to 1 (blue symbols in Figure 10) enhances the C_2H_2/HCN and HCN/H_2O molecular ratios, which is in line with our trends. In the framework of these models, BD disk atmospheres appear to have a lower O/C ratio (close to 1) than T Tauri disk atmospheres (see also Mandell et al. 2012 who find an O/C = 1.5 from the analysis of near-infrared C_2H_2 and HCN rovibrational bands in T Tauri disks). When oxygen is depleted relative to carbon, water abundances decrease while the abundance of hydrocarbons, especially C_2H_2 and CH_4, increase (Najita et al. 2011). Unfortunately, the high-resolution *Spitzer* spectrograph does not cover the rovibrational band of CH_4, and testing the inference of an enhanced carbon chemistry in BD disks will require additional observations. We also note that the CO_2 abundance decreases only slightly (by about a factor of two) when going from an O/C = 1.5 to 1, meaning that C_2H_2 and HCN remain more abundant than CO_2, in agreement with our finding.

Finally, we wish to discuss our results in the context of the proposed correlation between the strength of HCN/H_2O and the disk mass of T Tauri stars. Najita et al. (2013) attribute this correlation to higher disk masses producing more nonmigrating planetesimals that lock up water ice beyond the snow line, thereby decreasing the O/C ratio in the inner disk. Of our very-low-mass-star and BD disks, only three (#1, 3, and 4) have measured masses (Scholz et al. 2006). Their average disk mass is $\sim 10^{-3}$ $M_\odot$, which agrees with the disk mass over the stellar mass being about 1% throughout the M spectral type and down to the BD regime (Andrews et al. 2013; Mohanty et al. 2013). If BDs follow the trend proposed by Najita et al. (2013), we should have measured HCN/H_2O flux ratios as low as $\sim$0.6 for the water line at 17.22 μm,[8] indicating the prevalence of water vapor (high O/C ratio) in the inner region of low-mass disks. On the contrary, we find HCN/H_2O flux ratios all larger than 3 (see Figure 6), pointing to a depletion of water vapor in the inner regions of BD disks. Clearly, disks around very low mass stars and BDs do not follow the proposed trend between the HCN/H_2O flux ratio and the disk mass.

Could our observations still be explained with an analogous process, i.e., could low-mass BD disks have formed more nonmigrating icy planetesimals than T Tauri disks? As we mention in the Introduction, our BD sample may be slightly biased toward older objects with no strong jets or outflows. These disks may have had more time to produce large nonmigrating icy planetesimals than the perhaps younger sample of T Tauri disks discussed in the literature so far. Even for disks in the same star-forming region, there is growing observational evidence that the first steps of planet formation proceed faster in BD than in T Tauri disks at radial distances tracing the same disk temperature. First, 10 and 20 μm silicate emission features suggest that the warm (100–500 K, Juhász et al. 2009) atmospheres of BD disks contain, on average, larger grains than those of T Tauri disks (Pascucci et al. 2009; Riaz et al. 2012). Second, detailed SED modeling of "coeval" disks finds that disks around very low mass stars and BDs are more settled than disks around T Tauri stars, which also points to faster grain growth followed by dust settling (Szűcs et al. 2010). Finally, the detection of millimeter-sized grains in two young BD disks (Ricci et al. 2013) demonstrates that, even in the cold outer regions of these low-mass disks, large grains can form in a Myr timescale and be retained. The recent theoretical work of Pinilla et al. (2013) highlights some of the main physical processes that could contribute to the observed differences between BD and T Tauri disks. Pinilla et al. (2013) show that the growth timescale of micron-size particles due to settling is directly proportional to the square root of the stellar luminosity. This implies that small grains in BD disks grow an order of magnitude faster than those in T Tauri disks that trace regions at similar temperatures. At the same time, because the radial drift velocity is inversely proportional to the square root of the stellar mass, dust particles in BD disks are depleted faster than in T Tauri disks. While a mechanism to slow down the depletion of millimeter- or meter-size grains is needed in T Tauri disks (Pinilla et al. 2012), that mechanism must be more efficient in BD disks to explain the recent detections of millimeter dust particles. The models of Pinilla et al. (2013) support the view that the first steps of planet formation are faster in BD than in T Tauri disks. Unfortunately, these models do not follow the growth of dust up to planetesimals ($\sim$km in size), which is when gas drag does not significantly affect their orbital dynamics. Our inference of a lower O/C in BD disks than in T Tauri disks perhaps suggests that the faster dust growth in BD disks extends to the stage of nonmigrating planetesimals.

[8] Reading straight from Figure 3 of Najita et al. (2013), the HCN/H_2O flux ratio is $\sim$0.2 but the water flux there is measured for the 17 μm group, which includes three water lines (17.12, 17.22, and 17.36 μm). Our HCN/H_2O flux ratio is computed from the 17.22 μm H_2O line only, which contributes to about a third of the 17 μm group flux.

6. SUMMARY

We analyzed a unique dataset of high-resolution *Spitzer* spectra around eight very low mass star and BD disks. We report the first detections of Ne^+, H_2, CO_2, and tentative detections of H_2O toward these very faint and low-mass disks. Our main results can be summarized as follows.

1. Two of our [Ne II] 12.8 μm detections are likely tracing the hot (5000–10,000 K) surface of BD disks. [Ne II] line fluxes and upper limits, in combination with ancillary BD properties, suggest that X-rays, rather than EUV, are the main ionizing photons of BD disk atmospheres.
2. The H_2 $S(2)$ and $S(1)$ fluxes are consistent with an origin in the warm ($T \sim 600$ K) surface of BD disks. Hence, as in T Tauri disks, mid-infrared H_2 lines do not probe most of the disk mass.
3. The C_2H_2/HCN flux and column density ratios are, on average, higher for BD than for T Tauri disks, confirming the previous trend found in low-resolution *Spitzer* spectra (Pascucci et al. 2009).
4. The HNC/H_2O flux ratios are, on average, also higher for BD than for T Tauri disks. Our LTE modeling extends this result to column density ratios if mid-infrared H_2O lines trace warm ($T \geqslant 600$ K) gas.

While the larger C_2H_2/HCN ratio is well established when combining this and previous results, the larger HNC/H_2O column density ratio in BD disks is still tentative. Future observations with *JWST*/MIRI will be easily able to followup such faint disks and detect weak water lines or place much tighter constraints on the amount of water than what we could do with *Spitzer*/IRS.

We find that higher C_2H_2/HCN *and* HNC/H_2O ratios can be explained by disk models with a reduced O/C ratio in the inner disk. This low ratio may be linked to the formation of nonmigrating planetesimals locking up water beyond the snow line (Najita et al. 2011). In this scenario, BD "coeval" to T Tauri disks should be able to form more efficiently nonmigrating icy planetesimals. Dust observations and theoretical models suggest that the first steps of planet formation, up to the growth of millimeter-size grains, proceed faster in BD than in T Tauri disks. The observations we present here hint that this faster growth may extend to kilometer-size bodies.

The main implication of this scenario is that the inner regions of BD disks are overall "drier" than those of T Tauri disks. With an O/C ratio close to 1, the bulk composition of rocky planets around BDs should include large amounts of carbon phases (Bond et al. 2010) and be overall different from any terrestrial planet in our Solar System.

This work is based on observations made with the *Spitzer Space Telescope*, which is operated by the Jet Propulsion Laboratory, California Institute of Technology under a contract with NASA. I.P. acknowledges support from the NASA/ADP Grant NNX10AD62G. Basic research in infrared astrophysics at the Naval Research Laboratory is supported by 6.1 base funding.

Facilities: Spitzer, JWST

APPENDIX

BROADBAND FEATURES IN THE SPECTRUM OF 2MASS J16053215-1933159

The IRS low-resolution spectrum of 2MASS J16053215-1933159 (#7) is shown in Figure 11. Two broadband features

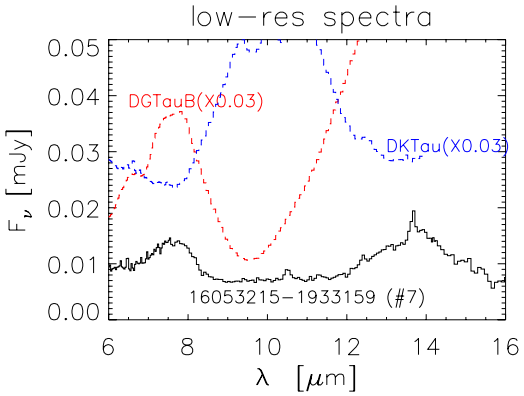

Figure 11. IRS low-resolution spectrum of 2MASS J16053215-1933159 (#7, solid black line). Red dashed line is the low-resolution spectrum of DG Tau B scaled by the factor in parenthesis. The low-resolution spectrum of DK Tau, scaled by the factor in parenthesis, is shown with a blue dashed line. Object 7 appears to have a shallow 10 μm silicate absorption feature indicative of a relatively high disk inclination and predominantly micron-size dust grains.

(A color version of this figure is available in the online journal.)

are present in this spectrum: one peaking around 7.5 μm and the other around 14 μm (this latter feature is also clearly detected in the IRS high-resolution spectrum, Figure 2). We have inspected the combined Nod1 and 2 images and found no evidence for extended emission at these wavelengths beyond the 3.″6 slit width. Hence, any observed emission is associated to the star/disk system. We have also searched the literature for known broadband dust emission features at these wavelengths but found none peaking at 7.5 and/or 14 μm. One possibility is that we are seeing this disk at relatively high inclination such that the prominent 10 μm silicate feature is seen in absorption, producing two apparent emission features shortward and longward of 10 μm. We have re-reduced many of the Taurus low-resolution spectra of disks available in the Spitzer Heritage Archive and found that the spectrum of the highly inclined disk (75°, Padgett et al. 1999) DG Tau B is the one that best resembles that of object 7 (see Figure 11, red dashed line, AOR: 25680128). The 10 μm absorption feature of DG Tau B is much narrower and deeper than that of object 7, reflecting the predominance of small, submicron-size dust grains (see also Kruger et al. 2011). Figure 11 also shows the IRS low-resolution spectrum of DK Tau (AOR: 3531264), a T Tauri disk with a prominent, but broad, 10 μm silicate emission feature indicative of micron-size dust grains in its atmosphere. Like DK Tau, the disk atmosphere of 2MASS J16053215-1933159 appears to be dominated by micron-size grains.

REFERENCES

Agúndez, M., Cernicharo, J., & Goicoechea, J. R. 2008, A&A, 483, 831
Alexander, R. D., Clarke, C. J., & Pringle, J. E. 2005, MNRAS, 358, 283
Alexander, R. D., Pascucci, I., Andrews, S., Armitage, P., & Cieza, L. 2013, in Protostars and Planets VI, ed. H. Beuther, C. Dullemond, Th. Henning, & R. Klessen (Tucson, AZ: Univ. Arizona Press), in press (arXiv:1311.1819)
Andrews, S. M., Rosenfeld, K. A., Kraus, A. L., & Wilner, D. J. 2013, ApJ, 771, 129
Baldovin-Saavedra, C., Audard, M., Carmona, A., et al. 2012, A&A, 543, A30
Banzatti, A., Meyer, M. R., Bruderer, S., et al. 2012, ApJ, 745, 90
Bond, J. C., Lauretta, D. S., & O'Brien, D. P. 2010, Icar, 205, 321
Bouwman, J., Henning, Th., Hillenbrand, L. A., et al. 2008, ApJ, 683, 479
Bouy, H., Hulamo, N., Pinte, C., et al. 2008, A&A, 486, 877
Carr, J. S., & Najita, J. R. 2008, Sci, 319, 1504
Carr, J., & Najita, J. 2011, ApJ, 733, 102
Ciesla, F., & Lauretta, D. 2005, E&PSL, 231, 1

de Zeeuw, P. T., Hoogerwerf, R., de Bruijne, J. H. J., Brown, A. G. A., & Blaauw, A. 1999, AJ, 117, 354
Espaillat, C., Ingleby, L., Furlan, E., et al. 2013, ApJ, 762, 62
Fedele, D., Pascucci, I., Brittain, S., et al. 2011, ApJ, 732, 106
Frenklach, M., & Feigelson, E. D. 1989, ApJ, 341, 372
Güdel, M., Briggs, K. R., Arzner, K., et al. 2007, A&A, 468, 353
Güdel, M., Lahuis, F., Briggs, K. R., et al. 2010, A&A, 519, A113
Gullbring, E., Hartmann, L., Briceno, C., & Calvet, N. 1998, ApJ, 492, 323
Hauschildt, P. H., Allard, F., & Baron, E. 1999, ApJ, 512, 377
Herczeg, G. J., & Hillenbrand, L. A. 2008, ApJ, 681, 594
Herczeg, G. J., Najita, J. R., Hillenbrand, L. A., & Pascucci, I. 2007, ApJ, 670, 509
Higdon, S. J. U., Devost, D., Higdon, J. L., et al. 2004, PASP, 116, 975
Hollenbach, D., & Gorti, U. 2009, ApJ, 703, 1203 (HG09)
Houck, J. R., Roellig, T. L., van Cleve, J., et al. 2004, ApJS, 154, 18
Howard, A. W., Marcy, G. W., Bryson, S. T., et al. 2012, ApJS, 201, 15
Juhász, A., Henning, Th., Bouwman, J., et al. 2009, ApJ, 695, 1024
Kenyon, S. J., Gómez, M., & Whitney, B. A. 2008, in Handbook of Star Forming Regions, Volume I: The Northern Sky ASP Monograph Publications, Vol. 4, ed. B. Reipurth (San Francisco, CA: ASP), 405
Klein, R., Apai, D., Pascucci, I., Henning, Th., & Waters, L. B. F. M. 2003, ApJL, 593, L57
Kress, M. E., Tielens, A. G. G. M., & Frenklach, M. 2010, AdSpR, 46, 44
Kominami, J., & Ida, S. 2002, Icar, 157, 43
Kruger, A. J., Richter, M. J., Carr, J. S., et al. 2011, ApJ, 729, 145
Lahuis, F., van Dishoeck, E. F., Blake, G. A., et al. 2007, ApJ, 665, 492
Lee, J.-E., Bergin, E. A., & Nomura, H. 2010, ApJL, 710, L21
Lissauer, J. J., & Stevenson, D. J. 2007, in Protostars and Planets V, ed. B. Reipurth, D. Jewitt, & K. Keil (Tucson, AZ: Univ. Arizona Press), 591
Luhman, K. L., Adame, L., D'Alessio, P., et al. 2007, ApJ, 666, 1219
Luhman, K. L., Allen, P. R., Espaillat, C., Hartmann, L., & Calvet, N. 2010, ApJS, 186, 111
Luhman, K. L., Stauffer, J. R., Muench, A. A., et al. 2003, ApJ, 593, 1093
Mandell, A. M., Bast, J., van Dishoeck, E. F., et al. 2012, ApJ, 747, 92
Meijerink, R., Pontoppidan, K. M., Blake, G. A., Poelman, D. R., & Dullemond, C. P. 2009, ApJ, 704, 1471
Meyer, M. R., Hillenbrand, L. A., Backman, D., et al. 2006, PASP, 118, 1690
Mohanty, S., Greaves, J., Mortlock, D., et al. 2013, ApJ, 773, 168
Muzerolle, J., Luhman, K. L., Briceño, C., Hartmann, L., & Calvert, N. 2005, ApJ, 625, 904
Morgan, W. A., Jr., Feigelson, E. D., Wang, H., & Frenklach, M. 1991, Sci, 252, 109
Nagasawa, M., Thommes, E. W., Kenyon, S. J., Bromley, B. C., & Lin, D. N. C. 2007, in Protostars and Planets V, ed. B. Reipurth, D. Jewitt, & K. Keil (Tucson, AZ: Univ. Arizona Press), 639
Najita, J. R., Ádámkovics, M., & Glassgold, A. E. 2011, ApJ, 743, 147
Najita, J. R., Carr, J. S., Pontoppidan, K. M., et al. 2013, ApJ, 766, 134
Najita, J. R., Doppmann, G. W., Bitner, M. A., et al. 2009, ApJ, 697, 957
Nomura, H., Aikawa, Y., Tsujimoto, M., Nakagawa, Y., & Millar, T. J. 2007, ApJ, 661, 334
Öberg, K. I., Murray-Clay, R., & Bergin, E. A. 2011, ApJL, 743, L16
Padgett, D. L., Brandner, W., Stapelfeldt, K. R., et al. 1999, AJ, 117, 1490
Papaloizou, J. C. B., & Terquem, C. 2006, RPPh, 69, 119
Pascucci, I., Apai, D., Luhman, K., et al. 2009, ApJ, 696, 143
Pascucci, I., Gorti, U., & Hollenbach, D. 2012, ApJL, 751, L42
Pascucci, I., Gorti, U., Hollenbach, D., et al. 2006, ApJ, 651, 1177
Pascucci, I., Hollenbach, D., Najita, J., et al. 2007, ApJ, 663, 383
Pascucci, I., & Sterzik, M. 2009, ApJ, 702, 724
Pascucci, I., Sterzik, M., Alexander, R. D., et al. 2011, ApJ, 736, 13
Pecaut, M. J., Mamajek, E. E., & Bubar, E. J. 2012, ApJ, 746, 154
Pinilla, P., Birnstiel, T., Benisty, M., et al. 2013, A&A, 554, A95
Pinilla, P., Birnstiel, T., Ricci, L., et al. 2012, A&A, 538, A114
Pontoppidan, K. M., Salyk, C., Blake, G. A., et al. 2010, ApJ, 720, 887
Rebull, L. M., Padgett, D. L., McCabe, C.-E., et al. 2010, ApJS, 186, 259
Riaz, B., Honda, M., Campins, H., et al. 2012, MNRAS, 420, 2603
Ricci, L., Isella, A., Carpenter, J. M., & Testi, L. 2013, ApJL, 764, L27
Ricci, L., Testi, L., Natta, A., Scholz, A., & de Gregorio-Monsalvo, I. 2012, ApJL, 761, L20
Rothman, L. S., Gordon, I. E., Barbe, A., et al. 2009, JQSRT, 110, 533
Sacco, G. G., Flaccomio, E., Pascucci, I., et al. 2012, ApJ, 747, 142
Salyk, C., Pontoppidan, K. M., Blake, G. A., Najita, J. R., & Carr, J. S. 2011, ApJ, 731, 130
Salyk, C., Pontoppidan, K. M., Blake, G. A., et al. 2008, ApJL, 676, L49
Schisano, E., Ercolano, B., & Gúdel, M. 2010, MNRAS, 401, 1636
Scholz, A., Jayawardhana, R., & Wood, K. 2006, ApJ, 645, 1498
Slesnick, C. L., Carpenter, J. M., & Hillenbrand, L. A. 2006, AJ, 131, 3016
Szűcs, L., Apai, D., Pascucci, I., & Dullemond, C. P. 2010, ApJ, 720, 1668S
Thi, W. F., van Dishoeck, E. F., Blake, G. A., et al. 2001, ApJ, 561, 1074
van Boekel, R., Güdel, M., Henning, Th., Lahuis, F., & Pantin, E. 2009, A&A, 497, 137
Walsh, C., Nomura, H., Millar, T. J., & Aikawa, Y. 2012, ApJ, 747, 114
Yang, H., Gregory, J., Linsky, J. L., et al. 2012, ApJ, 744, 121